CO2MVS RESEARCH ON SUPPLEMENTARY OBSERVATIONS

D2.7 Multi-scale global IFS inversion outputs (2021) with assimilated posterior emissions from hot-spots

Due date of deliverable	31-12-2025
Submission date	17-12-2025
File Name	CORSO-D2-7-v1.1
Work Package /Task	WP2 / Task 2.4
Organisation Responsible of Deliverable	ECMWF
Author name(s)	A. Visser, C. Schooling, N. Bousserez, P. Palmer.
Revision number	1
Status	Final
Dissemination Level / location	Public

The CORSO project (grant agreement No 101082194) is funded by the European Union.
Views and opinions expressed are however those of the author(s) only and do not necessarily reflect those of the European Union or the Commission. Neither the European Union nor the granting authority can be held responsible for them.

1 Executive Summary

This deliverable reports on the work performed in Task 2.4 of the CORSO project, where various inversion approaches were used to estimate CO_2 emissions at a range of different spatial scales.

First, this work reports on the implementation and further development of a posterior flux assimilation methodology, first proposed by Bousserez (2019), which enables the assimilation of external inversion products as observations in the Integrated Forecasting System (IFS). The assimilation method is first tested in a range of Observing System Simulation Experiments (OSSEs) to investigate the impact of ensemble size and a mis-represented prior uncertainty on the posterior uncertainty obtained by applying this method. From these OSSE experiments, we conclude that the posterior uncertainty is underestimated in small ensembles, and that an adaptive tuning procedure is required to correct for potential misrepresentations in the prior uncertainty.

We then apply this method to assimilate hotspot emission estimates into a posterior emission ensemble obtained from joint IFS Ensemble Data Assimilation and emission inversion experiments. In this case, hotspot NO_x emissions from selected power plants in the United States and Europe are converted to CO_2 emissions using a prior emission ratio and subsequently assimilated into an IFS emission ensemble. The required observational information (source rate, source rate uncertainty and hotspot location) is taken from CORSO Deliverable D2.2 (Kuhlmann et al., 2025). The assimilation results in an improved agreement with the assimilated observations and agrees reasonably well with independent emissions observations from Continuous Emissions Monitoring System (CEMS) for US power plants.

Second, this work develops a regional NO_x inversion framework that uses satellite NO_2 observations to constrain daily anthropogenic NO_x emissions over Europe for 2021. The GEOS-Chem model with a lightweight offline representation of NO_x chemistry is coupled to an Ensemble Kalman Filter (EnKF) system and constrained using high-quality TROPOMI NO_2 data. Emission uncertainties, spatial error correlations, and observation errors are explicitly represented, enabling robust and spatially resolved updates of NO_x fluxes across the European domain.

The optimised NO_x emissions are then used to directly update fossil-fuel CO_2 emissions through prescribed, sector-specific NO_x:CO_2 emission ratios. The assimilation significantly improves agreement between modelled and observed NO_2 and leads to a large reduction in uncertainty in European CO_2 emissions. The strongest corrections occur in southern and southeastern Europe, while northern and central regions show higher prior–posterior consistency. The resulting emissions exhibit enhanced wintertime fluxes and clear regional seasonal adjustments, demonstrating the potential of satellite NO_2 to provide powerful indirect constraints on anthropogenic CO_2 emissions.

This work has contributed to the development of the global CO2MVS with a first implementation of posterior flux assimilation described in the CO2MVS prototype methodology and by further developing a regional inversion system that could be used for regional benchmarking of the global emissions.

Table of Contents

2 Introduction

2.1 Background

To enable the European Union (EU) to move towards a low-carbon economy and implement its commitments under the Paris Agreement, a binding target was set to cut emissions in the EU by at least 40% below 1990 levels by 2030. European Commission (EC) President von der Leyen committed to deepen this target to at least 55% reduction by 2030. This was further consolidated with the release of the Commission's European Green Deal on the 11th of December 2019, setting the targets for the European environment, economy, and society to reach zero net emissions of greenhouse gases in 2050, outlining all needed technological and societal transformations that are aiming at combining prosperity and sustainability. To support EU countries in achieving the targets, the EU and European Commission (EC) recognised the need for an objective way to monitor anthropogenic CO_2 emissions and their evolution over time.

Such a monitoring capacity will deliver consistent and reliable information to support informed policy- and decision-making processes, both at national and European level. To maintain independence in this domain, it is seen as critical that the EU establishes an observation-based operational anthropogenic CO_2 emissions Monitoring and Verification Support (MVS) (CO2MVS) capacity as part of its Copernicus Earth Observation programme.

The CORSO research and innovation project will build on and complement the work of previous projects such as CHE (the CO2 Human Emissions), and CoCO2 (Copernicus CO2 service) projects, both led by ECMWF. These projects have already started the ramping-up of the CO2MVS prototype systems, so it can be implemented within the Copernicus Atmosphere Monitoring Service (CAMS) with the aim to be operational by 2026. The CORSO project will further support establishing the new CO2MVS addressing specific research & development questions.

The main objectives of CORSO are to deliver further research activities and outcomes with a focus on the use of supplementary observations, i.e., of co-emitted species as well as the use of auxiliary observations to better separate fossil fuel emissions from the other sources of atmospheric CO_2. CORSO will deliver improved estimates of emission factors/ratios and their uncertainties as well as the capabilities at global and local scale to optimally use observations of co-emitted species to better estimate anthropogenic CO_2 emissions. CORSO will also provide clear recommendations to CAMS, ICOS, and WMO about the potential added-value of high-temporal resolution $^{14}CO_2$ and APO observations as tracers for anthropogenic emissions in both global and regional scale inversions and develop coupled land-atmosphere data assimilation in the global CO2MVS system constraining carbon cycle variables with satellite observations of soil moisture, LAI, SIF, and Biomass. Finally, CORSO will provide specific recommendations for the topics above for the operational implementation of the CO2MVS within the Copernicus programme.

2.2 Scope of this deliverable

2.2.1 Objectives of this deliverable

In this deliverable, we:

1. Introduce and test a posterior flux assimilation methodology to assimilate hotspot emission estimates from native-resolution satellite observations into a posterior emission ensemble.
2. Apply the posterior flux assimilation algorithm to derive updates to power plant CO_2 emissions in the United States and Europe and compare these estimates to power plant-reported data and an independent inversion framework.
3. Incorporate the parametrised NO_x chemistry scheme into GEOS-Chem to apply Ensemble Kalman Filter (EnKF) assimilation of to update European prior fluxes for 2021.

2.2.2 Work performed in this deliverable

1. Implemented a posterior flux assimilation algorithm to correct posterior IFS CO_2 emissions based on hotspot emissions derived from TROPOMI NO_2 observations.
2. Testing of the posterior flux assimilation in a set of Observing System Simulation Experiments (OSSEs).
3. Application of the posterior flux assimilation algorithm for June and December 2021 for selected power plants in the United States and Europe.
4. Implemented EnKF assimilation of TROPOMI NO_2 in GEOS-Chem to constrain European NO_x emissions for 2021.
5. Derived updated CO_2 combustion fluxes from the EnKF posterior NO_x emissions using prescribed NO_x:CO_2 ratios.
6. Quantified improvements in model–observation agreement and CO_2 emission uncertainty reduction.
7. Comparison of posterior emissions between the hotspot assimilation algorithm and GEOS-Chem for 5 power plants in Europe.

2.2.3 Deviations and counter measures

No deviations

2.3 Project partners:

Partners	
EUROPEAN CENTRE FOR MEDIUM-RANGE WEATHER FORECASTS	ECMWF
AKADEMIA GORNICZO-HUTNICZA IM. STANISLAWA STASZICA W KRAKOWIE	AGH
BARCELONA SUPERCOMPUTING CENTER - CENTRO NACIONAL DE SUPERCOMPUTACION	BSC
COMMISSARIAT A L ENERGIE ATOMIQUE ET AUX ENERGIES ALTERNATIVES	CEA
KAMINSKI THOMAS HERBERT	iLab
METEO-FRANCE	MF
NEDERLANDSE ORGANISATIE VOOR TOEGEPAST NATUURWETENSCHAPPELIJK ONDERZOEK TNO	TNO

RIJKSUNIVERSITEIT GRONINGEN	RUG
RUPRECHT-KARLS-UNIVERSITAET HEIDELBERG	UHEI
LUNDS UNIVERSITET	ULUND
UNIVERSITE PAUL SABATIER TOULOUSE III	UT3-CNRS
WAGENINGEN UNIVERSITY	WU
EIDGENOSSISCHE MATERIALPRUFUNGS- UND FORSCHUNGSANSTALT	EMPA
EIDGENOESSISCHE TECHNISCHE HOCHSCHULE ZUERICH	ETHZ
UNIVERSITY OF BRISTOL	UNIVBRIS
THE UNIVERSITY OF EDINBURGH	UEDIN

3 Posterior flux assimilation methodology

3.1 Input data

3.1.1 Hotspot emission estimates derived from TROPOMI

We assimilate hotspot emission estimates derived in CORSO Deliverable D2.2 (Kuhlmann et al. 2025), which contains daily NO_x emissions for the power plants in the top 100 list of strongest emitting point sources in the CORSO point source database (Guevara et al. 2024), considering only those power plants sufficiently far from other emission sources. In this analysis, we focus on the United States and Europe, since power plants in these regions have Continuous Emissions Monitoring Systems (CEMS) for monitoring compliance with air quality regulations. These data are used for validation, and are further described in Section 3.1.3. In total, 17 power plants in the United States and Europe fulfil these criteria. Figure 1 displays the yearly average NO_x emissions for these power plants.

The hotspot emission estimates are derived from NO_2 observations from the TROPOspheric Monitoring Instrument (TROPOMI) onboard Sentinel-5P (Veefkind et al. 2012).The NO_x emissions were estimated using NO_2 observations from individual TROPOMI overpasses using the cross-sectional flux method, which estimates emissions by integrating the NO_2 mass through cross-sections of an emission plume, and multiplying by the wind speed taken from ERA5 (Hersbach et al. 2020) to obtain an emission rate. This method accounts for NO_2-to-NO_x conversion and NO_x decay. More details can be found in Kuhlmann et al. (2025).

Prior to assimilation, we convert the NO_x hotspot emission estimates to CO_2 by applying a CO_2:NO_x emission ratio (ER), derived from the IFS prior (CAMS-GLOB-ANT, version 6.2; Soulie et al. 2024). The CO_2 emission uncertainty is derived by applying error propagation using the hotspot NO_x emission uncertainty and an assumed ER uncertainty. We use a relative ER uncertainty of 42% derived from satellite observations (Kuhlmann et al. 2021, Liu et al. 2020). An example of this conversion is shown in Figure 2. We note that this uncertainty estimate is likely to be conservative given the uncertainties involved in estimating this ratio from satellite observations (e.g. due to the retrieval algorithm and atmospheric chemistry). On the other hand, since CO_2 and NO_x emissions are correlated, part of the uncertainty in the prior emission ratio cancels, which is not accounted for in this satellite-derived ER uncertainty estimate.

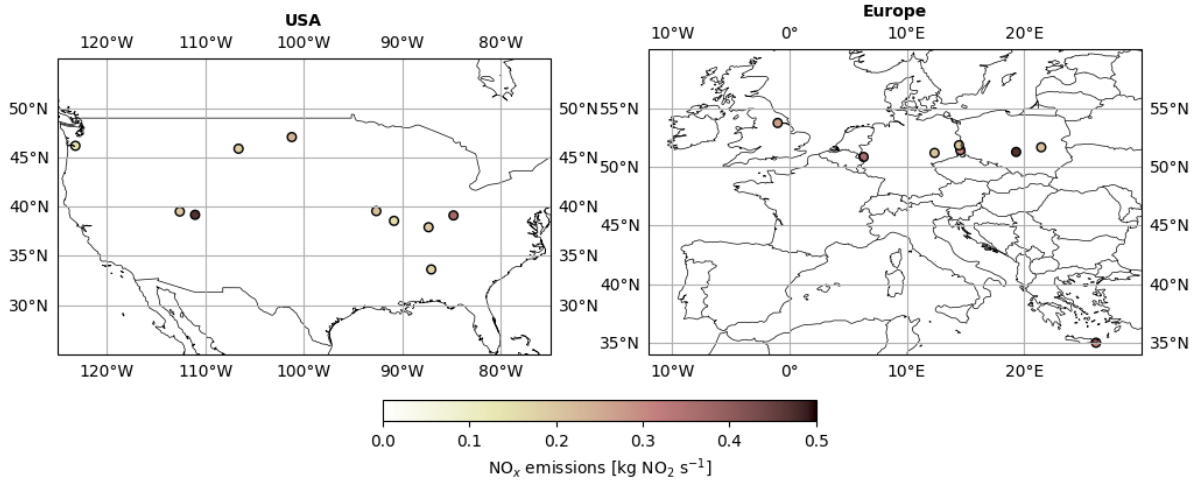

Figure 1. Locations of the energy sector emission hotspots in the United States (left panel) and Europe (right panel) used for assimilation in this study. The circle colour reflects the annual average NO_x emissions derived based on TROPOMI observations.

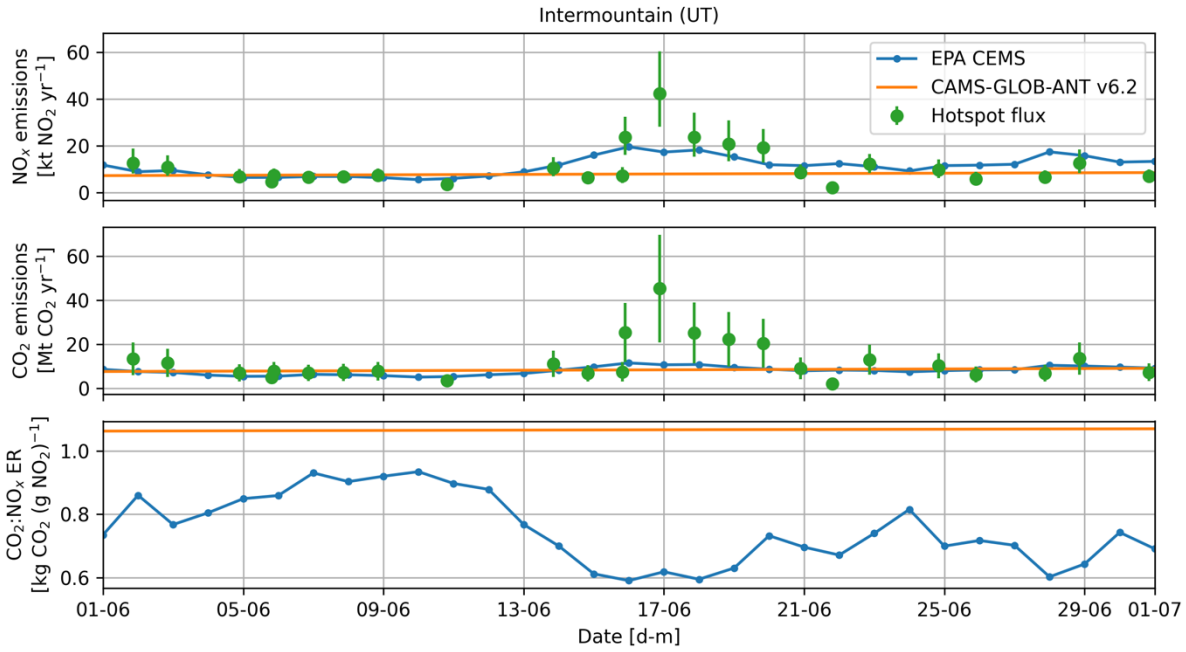

Figure 2. NO_x emissions (upper panel), CO_2 emissions (centre panel) and the CO_2:NO_x emission ratio (lower panel) for the Intermountain power plant in Utah, USA, from three different data sets: the United States Environmental Protection Agency's Continuous Emission Monitoring System (EPA CEMS, blue), the CAMS-GLOB-ANT emission inventory v6.2 (orange) and the TROPOMI-derived NO_x emissions derived using the cross-sectional flux method (green). Hotspot CO_2 emissions were derived from hotspot NO_x emissions as described in Section 3.1.1.

3.1.2 IFS ensemble emission inversion experiments

3.1.2.1 IFS forward model

The Integrated Forecasting System (IFS) is used operationally at ECMWF for Numerical Weather Prediction (NWP) and for monitoring and forecasting air pollution and greenhouse gases as part of the Copernicus Atmosphere Monitoring Service (CAMS) (Flemming et al., 2015, Agustí-Panareda et al., 2022). For this deliverable, we apply the IFS greenhouse gas configuration. The model has 137 hybrid sigma-pressure levels from the surface to 0.1 hPa with a vertical resolution that varies with (geometric) altitude, peaking in the planetary boundary layer. Tracer advection is calculated with a semi-Lagrangian scheme (Diamantakis and Magnusson, 2016), and a mass fixer is subsequently applied to ensure mass conservation (Agustí-Panareda et al., 2017). The transport model additionally includes parameterizations of turbulent mixing (Sandu et al., 2013) and convection (Bechtold et al., 2014). The forward model is run on a cubic octahedral $T_{co}399$ grid with an approximate horizontal resolution of 25 km, using a time step of 15 minutes.

3.1.2.2 IFS Ensemble Data Assimilation + inversion framework

The posterior flux assimilation method relies on an ensemble of emissions, which in this case is derived from Ensemble Data Assimilation (EDA) inversion experiment with the Integrated Forecasting System. EDA has been used operationally at ECMWF since 2010, and its applicability for greenhouse gas state optimization has recently been investigated. The IFS inversion framework is based on the 4D-Var data assimilation system implemented in IFS (Courtier et al. 1994, Rabier et al. 2000). In an emission inversion context, the 4D-Var state vector is extended with a 2D multiplicative emission scaling factor such that IFS jointly optimizes meteorology, the atmospheric state and emissions, using the following cost function:

$$J(\mathbf{x},\mathbf{p}) = (\mathbf{x}-\mathbf{x_b})^{T}\mathbf{B_x^{-1}}(\mathbf{x}-\mathbf{x_b}) + (\mathbf{p}-\mathbf{p_b})^{T}\mathbf{B_p^{-1}}(\mathbf{p}-\mathbf{p_b}) + \big(\mathbf{y}-h(\mathbf{x},\mathbf{p})\big)^{T}\boldsymbol{R^{-1}}(\mathbf{y}-h(\mathbf{x},\mathbf{p})). \quad (1)$$

The cost function is minimized with respect to state vectors $\mathbf{x}$ (meteorological variables and atmospheric concentrations) and $\mathbf{p}$ (emission scaling factors). $\mathbf{B}_x$ and $\mathbf{B_p}$ represent the background and prior error covariance matrices, respectively, and $\mathbf{R}$ is the observation error covariance matrix. A previous version of the IFS inversion framework has been described in McNorton et al. (2022).

The IFS inversion system currently optimizes total (anthropogenic) surface fluxes using a single 2D scaling factor field per species. The posterior emissions are optimized using three inner-loop minimizations at different resolutions (~125 km, ~100 km and ~80 km) within a 12-hour assimilation window. Posterior scaling factors from these inversions are applied to the prior emissions on a grid of ~25 km resolution. We use an ensemble with one control member and ten perturbed members, initialized with a uniform prior uncertainty of 30% and a spatially uniform correlation length scale of 100 km. The current inversion configuration assumes no time correlation between emission adjustments in consecutive assimilation windows, which may lead to spurious day-to-day variability in posterior emissions. The prior error covariance matrix setup will be further tested as part of the CO2MVS ramp-up in the coming period.

One application of the EDA is to provide a flow-dependent estimate of the background error covariance matrix $\mathbf{B}_x$. The EDA generates spread by applying random perturbations to the assimilated observations, the model physics during the forward model integration, and sea surface temperature. The emissions in the perturbed EDA ensemble members were generated by multiplying the square root $\mathbf{L}$ of the prior error covariance matrix ($\mathbf{B_p} = \mathbf{L_p}\mathbf{L_p^{\mathrm{T}}}$) to a two-dimensional field with random values ($\mathbf{v}$):

$$\mathbf{p_b'} = \mathbf{L_p}\mathbf{v}. \quad (2)$$

This ensures that the emission perturbations are consistent with the prior error specification for the emission scaling factors in each assimilation window.

3.1.3 Validation data: United States power plant-reported emissions

We use Continuous Emission Monitoring System (CEMS) data from the United States Environmental Protection Agency's Clean Air Market Program Data portal (EPA, 2025). In this dataset, direct stack measurements of NO_x, CO_2 (among other pollutants) are reported for power plants in the United States. This type of data has been previously used in inverse modelling of CO_2 emissions based on satellite NO_2 observations (Liu et al., 2020). CEMS data is available at high temporal resolution (hourly or daily) and are thus well suited to evaluate the impact of hotspot emission assimilation on temporal emission variability. We use daily aggregated CEMS data as an independent validation of the assimilated hotspot emission product. An example daily time series of EPA CEMS data is shown in Figure 2.

3.2 Posterior flux assimilation algorithm

Following Bousserez (2019), we apply a Kalman filter update algorithm to assimilate TROPOMI-derived posterior emissions from hotspots ($\boldsymbol{x_r}$) in prior ensemble member m ($\boldsymbol{z_{b,m}}$) to yield the updated ensemble member $\boldsymbol{z_{a,m}}$:

$$\boldsymbol{z_{a,m}} = \boldsymbol{z_{b,m}} + \frac{1}{N-1}\boldsymbol{Z_b}(\boldsymbol{AZ_b})^{T}\left(\frac{1}{N-1}\boldsymbol{AZ_b}(\boldsymbol{AZ_b})^{T} + \boldsymbol{E}\right)^{-1}(\boldsymbol{x_r} - \boldsymbol{Az_{b,m}}), \quad (3)$$

where N is the ensemble size, $\boldsymbol{Z_b}$ is the prior ensemble of emission anomalies with respect to the control member $\boldsymbol{z_{b,0}}$, $\boldsymbol{A}$ is the averaging kernel mapping the ensemble (member) to

observation space, and $\boldsymbol{E}$ is a diagonal matrix containing hotspot emission uncertainties (expressed as σ^2).

The prior ensemble (derived from the IFS emission inversion algorithm) may contain long-distance correlations, which can be caused by the small ensemble size. This results in spurious posterior increments (the right-hand term in Equation (3)) far from the location of the hotspot after applying the above equation. To localize these emission increments, we apply Gaspari-Cohn localization (Gaspari and Cohn, 1999) to the posterior emission update. Sensitivity tests with a varying localization radius yields an optimum value of 10 km.

The IFS ensemble spread in $\boldsymbol{Z_b}$ is not necessarily representative of the true prior error standard deviation. This could be due to a misrepresentation in the magnitude or temporal variability of the prior emission. In extreme cases, this can result in first-guess departures of up to several magnitude in extreme cases. To ensure a representative prior ensemble spread required for assimilating hotspot fluxes, we apply an objective tuning method based on a χ^2 diagnostic. This method relies on evaluating the cost function of the assimilation algorithm, which has the following property:

$$\mathbb{E}\left[J(\boldsymbol{z_{a,m}})\right] = p \tag{4}$$

where p is the number of observations (1 in this case), and $J(\boldsymbol{z_{a,m}})$ is the cost function evaluated for the posterior emission estimate. After applying a Gaspari-Cohn localization, which filters the sampling noise by restricting the emission increments around the assimilated hotspot, the control vector space can be reduced to the local subspace with non-zero posterior emission increments ($\boldsymbol{z'_a}$). This enables to reduce the dimension of the problem and explicitly invert $\mathbf{B}$. We write the cost function in the reduced space as follows:

$$J[\boldsymbol{z_a}'] = \frac{1}{2}\left(\boldsymbol{z'_{a,m}} - \boldsymbol{z'_{b,m}}\right)^T \boldsymbol{B'^{-1}}\left(\boldsymbol{z'_{a,m}} - \boldsymbol{z'_{b,m}}\right) + \frac{1}{2}\left(\boldsymbol{x_r} - \boldsymbol{A z_{a,m}}\right)^T \boldsymbol{E^{-1}}\left(\boldsymbol{x_r} - \boldsymbol{A z_{a,m}}\right) \tag{5}$$

where z'_b is the prior ensemble member m in the subspace with non-zero emission increments, and

$$\boldsymbol{B'} = \boldsymbol{Z'_b}(\boldsymbol{Z'_b})^T = \boldsymbol{S Z_b Z_b^T S^T} \tag{6}$$

is the prior error covariance matrix, restricted to this subspace by applying a selection matrix $\boldsymbol{S}$. The initial guess for the relative error σ_b is defined as:

$$\sigma_b = \frac{|\boldsymbol{A z_{b,m}} - \boldsymbol{x_r}|}{|\boldsymbol{A z_{b,m}}|}, \tag{7}$$

and this value is used to update $\boldsymbol{B'}$. A fixed-point algorithm can be used to find the solution to Equation (4), i.e. $J[\boldsymbol{z_{a,m}}] \approx n_{obs}$ (see, e.g., Chapnik et al., 2006).

We note that the iterative adaptive tuning of σ_b based on minimization of J is not yet implemented. As a preliminary test, we currently use the initial guess for σ_b (Equation (7)) in the assimilation procedure. This does not necessarily result in reaching $J[\boldsymbol{z_{a,m}}] \approx n_{obs}$. As a result, the current version of the algorithm does not always produce optimal results in terms of posterior uncertainty reduction. We evaluate the performance of the current assimilation algorithm in Section 4.1.

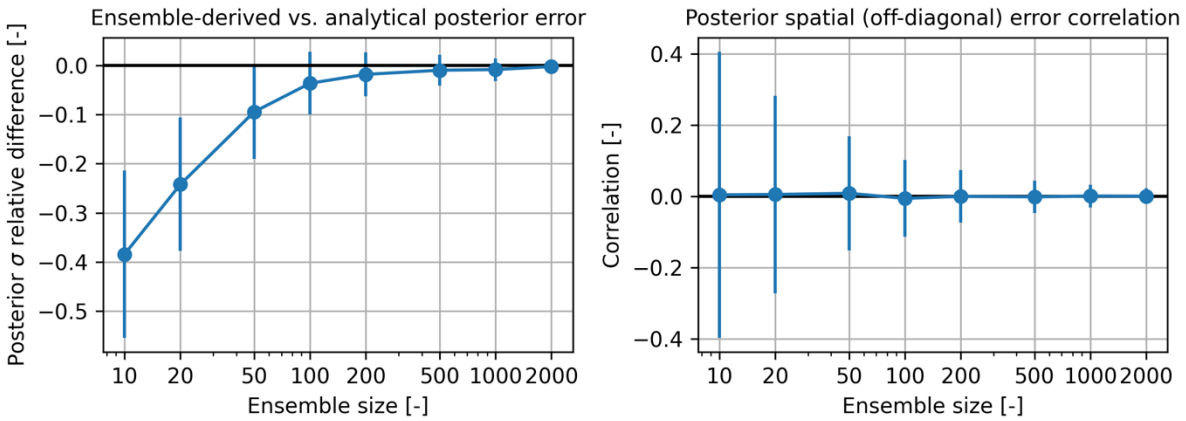

Figure 3. Summary statistics of the first OSSE experiment. Left panel: relative difference between the ensemble derived and analytical posterior (calculated as $(\boldsymbol{P_a^e} - \boldsymbol{P_a^t})/\boldsymbol{P_a^t}$) as a function of ensemble size. Points and error bar refer to the average and ±1σ range, respectively, calculated at the locations of the 50 assimilated observations. Right panel: spatial error correlation in the posterior error covariance matrix, displayed as the average (points) and ±1σ range derived from a 1000-member sample of off-diagonal elements in $\boldsymbol{P_a^e}$.

3.3 Algorithm validation Observing System Simulation Experiments

3.3.1 Posterior uncertainty as a function of ensemble size

We validate the implementation of this algorithm by evaluating the posterior error reduction in Observation System Simulation Experiments (OSSEs), and by studying its ability to recover the theoretical posterior error for different ensemble sizes. The theoretical posterior error covariance matrix ($\boldsymbol{P_a^t}$) can be approximated as:

$$\boldsymbol{P_a^t} = \left(\boldsymbol{B^{-1}} + \boldsymbol{A^T E^{-1} A}\right)^{-1}, \tag{8}$$

where $\boldsymbol{B}$ is the prior error covariance matrix, and the other terms as defined for Equation (3). An estimate of the posterior error can also be derived from the posterior ensemble:

$$\boldsymbol{P_a^e} = \frac{1}{N-1}\boldsymbol{Z_a Z_a^T}, \tag{9}$$

where $\boldsymbol{Z_a}$ is the posterior ensemble of anomalies with respect to the ensemble mean. Due to sampling noise, $\boldsymbol{P_a^e}$ and $\boldsymbol{P_a^t}$ may differ especially for small ensembles. With this OSSE setup, we study the properties of the posterior error covariance approximation as a function of ensemble size.

For this experiment, we construct synthetic ensembles of uncorrelated Gaussian noise with mean 100 (unitless) and a prior error standard deviation of 20%, using a coarse spatial resolution (1000 grid cells). Synthetic emission observations ($n_{obs} = 50$) are sampled from the control member and perturbed with an observation uncertainty of 40%. These observations are assimilated in the synthetic ensemble using Equation (3).

Figure 3 shows the dependence of the posterior uncertainty and spatial error correlation as a function of ensemble size. The ensemble-derived posterior uncertainty, shown in Figure 3 (left panel) is underestimated for small ensembles, by up to 40% for a 10-member ensemble. This underestimation is reduced as the ensemble size increases, following theoretical expectations. These ensembles agree within 1 standard deviation for ensembles of size 100 or larger. To avoid overfitting of the observations, a sufficiently large ensemble size must be chosen. Spatial error correlation is present in the posterior error covariance matrix due to sampling noise. On average, the spatial error correlation is near-zero for all tested ensemble sizes (Figure 3, right panel). Nonetheless, substantial off-diagonal noise is present in $\boldsymbol{P_a^e}$ for small ensembles, which decreases towards zero for the larger ensemble sizes tested in this

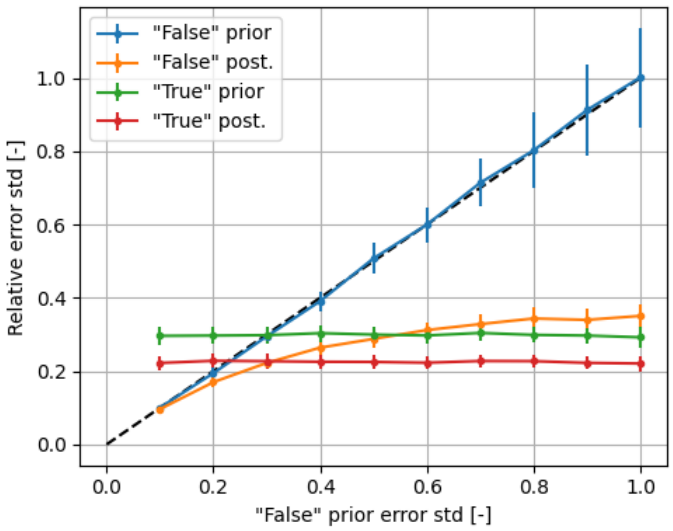

Figure 4. Relative prior and posterior error standard deviation in the OSSE experiment to investigate the impact of wrongly specified prior uncertainties, shown as a function of the "false" prior uncertainty.

study. Based on this OSSE analysis, we conclude that the implementation of the Kalman filter assimilation algorithm introduced behaves according to theoretical expectations, and that sufficiently large ensembles are required to minimize underestimation of the posterior uncertainty and spurious spatial error correlation.

3.3.2 Impact of mis-prescribed prior uncertainties

In a second OSSE experiment, we test the ability of the posterior flux update algorithm without adaptive tuning of σ_b to correct for a wrongly specified prior uncertainty. For this OSSE, we generate 50 synthetic observations from a 100-member prior ensemble with a correctly specified, or "true", prior uncertainty of 30%. These observations are perturbed using an observation uncertainty of 30%. In a second ensemble, referred to as the "false" ensemble, the prior uncertainty (expressed as a relative standard deviation) is incorrectly specified at values ranging from 0.1-1 with increments of 0.1. The same synthetic observations (sampled from the "true" prior ensemble) are assimilated into this ensemble. The results are displayed as a function of the "false" prior uncertainty in Figure 4.

In this OSSE experiment, the "true" posterior uncertainty is reduced compared to the prior as expected. The posterior uncertainty is underestimated when starting from an underestimated prior uncertainty. When the "false" prior uncertainty is larger than the "true" prior uncertainty, the "false" posterior uncertainty is corrected downward, and seems to plateau as the "false" prior uncertainty increases. We conclude that an adaptive tuning of σ_b is required prior to assimilation in order to recover the "true" posterior uncertainty when starting from a wrongly specified prior uncertainty.

3.4 EnKF inversion experiments

3.4.1 GEOS-Chem offline NO_x chemistry model

We use version 14.4.3 of the GEOS-Chem atmospheric chemistry transport model (Bey et al., 2001). Our simulations use the nested-grid carbon configuration, into which we incorporate NO_x species by implementing a lightweight offline treatment of NO_x chemistry. The chemistry rates are calculated using offline chemistry fields saved from a full chemistry simulation and works on the principle that the instantaneous effective lifetime of NO_x across space and time is assumed to be unchanged under emission perturbations (Schooling et al. 2025).

The nested model is centred over mainland Europe (32.75 to 61.25° N, -15 to 40° E) with 47 vertical levels, and a horizontal spatial resolution of 0.25°x0.3125°. Lateral boundary conditions to the European domain were created from a global GEOS-Chem model run at 4×5°, with three-hourly output fields. The nested model was run with a 5-minute transport timestep and 10-minute chemistry timestep.

The model is driven by offline meteorological fields from the GEOS-FP dataset provided by NASA's Global Modelling and Assimilation Office (GMAO), with a native resolution of 0.25°x0.3125°, 72 vertical levels, and 3-hourly temporal resolution. The prior fluxes for combustion emissions of NO_x and CO_2 are taken from the CAMS_REG v8.1 emissions inventory (Hohenberger et al., 2025, Figure 5) at 0.1x0.05° resolution. Temporal variability in emissions (monthly, daily, hourly) are represented using sector-based temporal scaling factors (Figure 5b). The combustion sectors included are public power, industry, road transport, ships, aviation, off-road machinery, and other combustion sources. The CO_2:NO_x emission ratio is prescribed for each of these combustion sector, allowing the combustion-based NO_x fluxes to be converted into $ffCO_2$ flux estimates. Non combustion sources, including solvents, waste, agriculture, and fugitive emissions, are prescribed as fixed within the data assimilation. In addition, the NO_x emissions from soil, lightning, and biomass burning are parameterised within GEOS-Chem (Vinken et al. 2014, Gressent et al. 2016).

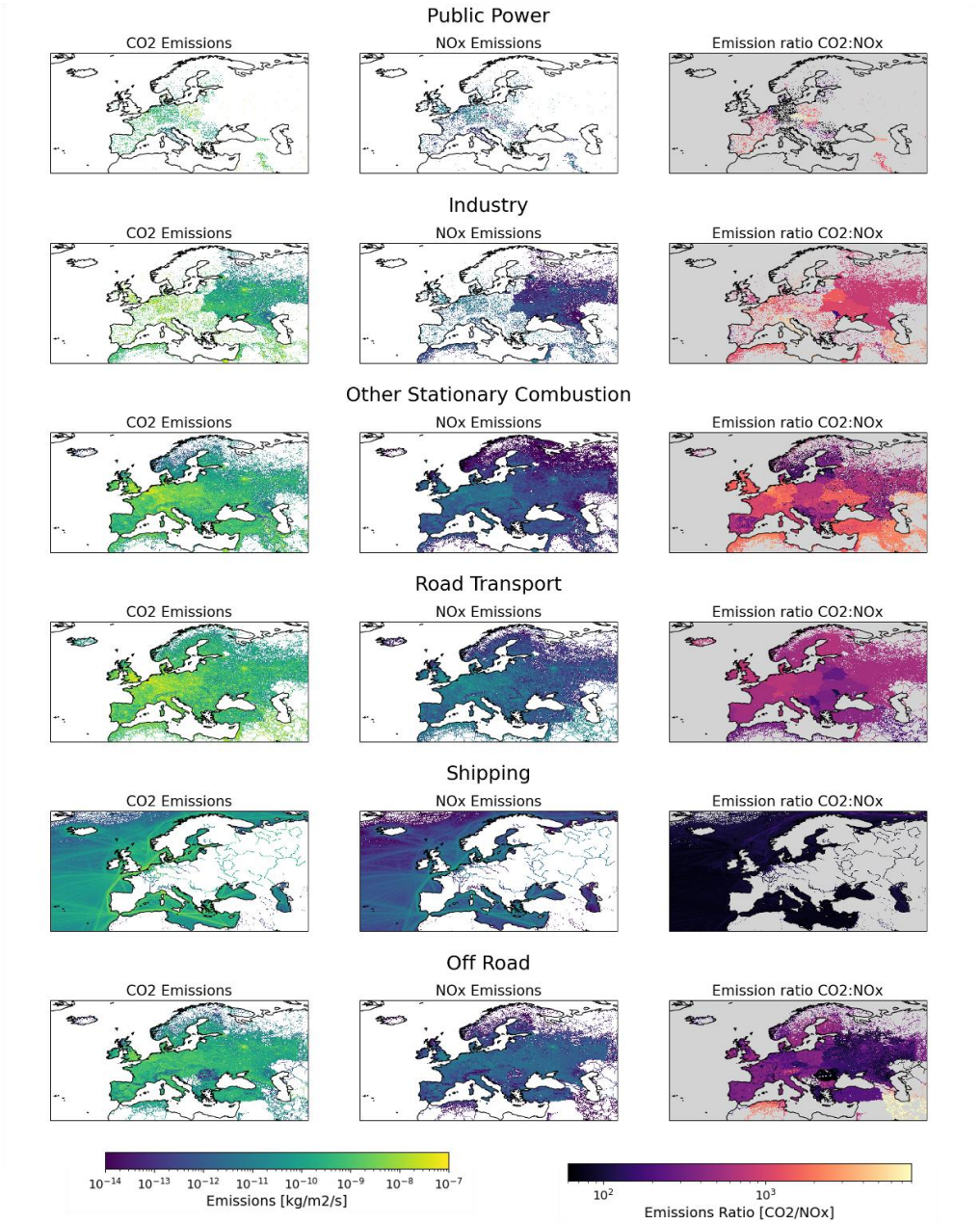

(a)

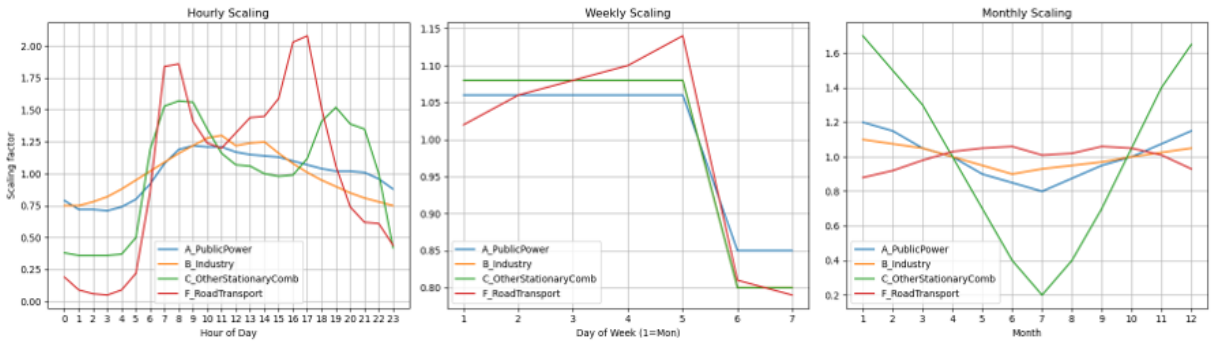

(b)

Figure 5. (a) The 2021 CAMS-REG v8.1 emissions data for CO2, NOx, and their respective ratio across the main combustion sectors. **(b)** The temporal profiles applied to the Public Power, Industry, Other Stationary Combustion, and Road Transport sectors.

3.4.2 TROPOMI observations

We used satellite observations of NO_2 from the TROPOspheric Monitoring Instrument (TROPOMI) to constrain anthropogenic NO_x emissions over Europe. We use v2.4.0 data for the full year 2021. TROPOMI provides daily global coverage with a local equatorial overpass time of 13:30, a 2,600 km swath, and 7x7 km^2 nadir resolution. We select only high-quality retrievals with a quality assurance value, *qa*>0.75. The data was resampled onto the GEOS-Chem 0.25°x0.3125° grid, and the satellite averaging kernels were interpolated onto the 47 vertical levels of the model to compute vertically sensitive model column densities.

In our European region following filtering with quality assurance, the daily and monthly coverage of observations for the year 2021 are shown in Figure 6. The coverage has clear seasonal dependence, with mean daily coverage of around 45% in winter (DJF) and 70% in summer (JJA).

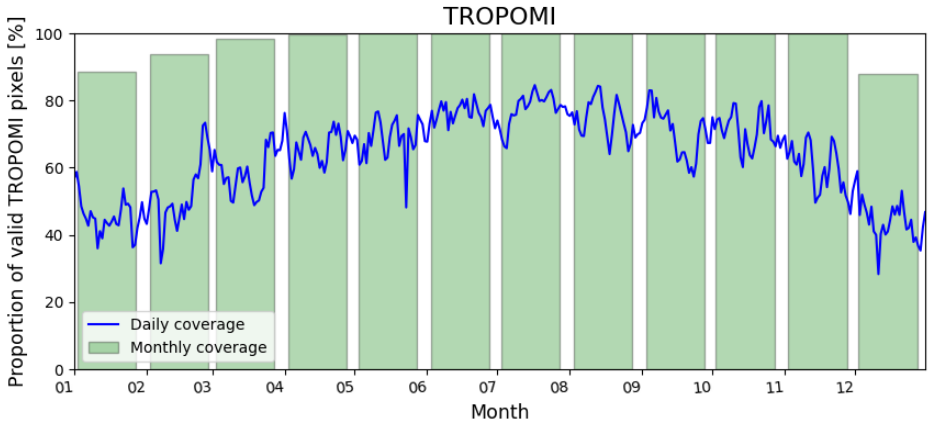

Figure 6. The daily and monthly proportional coverage of TROPOMI NO_2 over GEOS-Chem pixels in the European domain for 2021. Coverage is defined as the proportion of GEOS-Chem grid cells across the European domain that receive at least one valid TROPOMI observation within the specified time period. Thus, 100% daily coverage means every grid cell was observed at least once during the period (day or month).

3.4.3 Ensemble Kalman Filter (EnKF) procedure

We use an existing EnKF framework that has been widely used to estimate CO_2 and CH4 fluxes from atmospheric observations (Feng et al. 2009, 2017). In this implementation, we assimilate satellite-based NO_2 column observations (y_{obs}), to update the prior flux state vector (x^f) and produce the posteriori state vector (x^a) using the standard Kalman filter formulation:

$$x^a = x^f + K\left[y_{obs} - Hx^f\right], \quad (10)$$

where H is the observation operator that maps the state vector to observation space, and K is the Kalman gain matrix.

In the ensemble approach, we introduced an ensemble of N=100 perturbation states. The ensemble prior error covariance matrix (Σ) was constructed using the CAMS-REG v8.1 emission uncertainties (σ_n, σ_c) together with the cross-species error correlation product (*r*):

$$\Sigma = \begin{pmatrix} \sigma_n^2 & r\sigma_n\sigma_c \\ r\sigma_n\sigma_c & \sigma_c^2 \end{pmatrix} . \quad (11)$$

We generated an ensemble of NO_x emission scaling's by sampling from a bivariate normal distribution, N(0, Σ) at each grid cell. This produces spatially resolved perturbations that preserve both the magnitude of uncertainties and the correlation between NO_x and CO_2 errors (Figure 7).

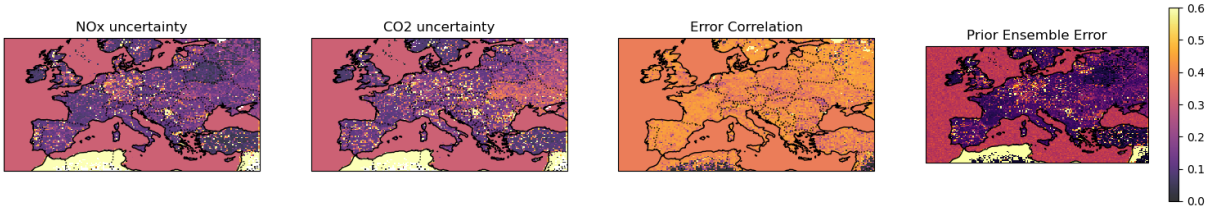

Figure 7. NO_x and CO_2 uncertainties (σ_n, σ_c) from CAMS-REG v8.1 emissions, the cross-species error correlation product (r), taken from the global CORSO product, and the prior ensemble errors calculated from the prior error covariance matrix (Σ).

The forward-modelled NO_2 columns from each ensemble member (denoted $H(x^f)$) are compared to satellite retrievals to compute the innovation vector $d = y_{obs} - H(x^f)$. We apply a spatial mask to exclude edge regions and measurement outliers. The Kalman gain matrix is then estimated using the ensemble approximation (Feng et al. 2009, 2017):

$$K \approx \Delta X^f \left(\Delta Y^f\right)^T \left[\Delta Y^f \left(\Delta Y^f\right)^T + R\right]^{-1}, \quad (12)$$

where ΔY^f represents the ensemble of deviations in the observation space, and R is the observation error covariance matrix. To reduce the impact of spurious long-range correlations, we applied localisation to the Kalman gain. We compute the distance between each grid cell and each valid observation, and apply a Gaussian tapering function $exp(-d_{ij}/L)$ with a correlation length scale L = 200 km. This localisation is applied multiplicatively to the Kalman gain, element-wise.

In our setup, R is defined as a diagonal matrix that incorporates satellite retrieval uncertainty using the TROPOMI precision values, and includes a fixed model error of 1×10^{13} molecules (molec)/cm^2, corresponding to the average reconstruction error of NO_2 columns derived from scaled offline chemistry (Schooling et al. 2025). Additionally, we applied an adaptive inflation scheme that increased the observation error covariance by a factor of 10 whenever the observed values significantly differ from the model predictions ($|d|>2\times10^{16}$ molec/cm^2). Furthermore, an additional constraint was applied to ensure the posterior flux estimates are always greater than zero.

To quantify the change in model agreement with observations as the fluxes are updated to posterior we assess the coefficient of determination (R^2), the mean bias, mean absolute error (MAE), and the error variance reduction (EVR), defined as:

$$EVR = 100\,x\left(1 - \frac{\sigma^2_{post}}{\sigma^2_{prior}}\right), \quad (13)$$

where σ^2_{prior}, σ^2_{post} are the variances of the prior and posterior model errors, respectively. Since NO_x is short-lived observations are generally insensitive to emission changes from previous days so we use a data assimilation window of one day. Due to the non-linearity of NO_x emissions with atmospheric NO_2 observations, it is possible to maximise error reduction by

repeating the ensemble runs multiple times in an iterative procedure. Up to 4 iterations were performed, however the procedure was broken early if the percentage reduction in mean absolute error falls below 1, suggesting a plateau in model improvement.

4 Results

4.1 Impact of hotspot assimilation on power plant CO_2 emissions

The impact of the posterior flux hotspot assimilation procedure is shown for the Intermountain (Figure 8) and Thomas Hill (Figure 9) power plants in the United States, where prior and posterior fluxes are compared against power plant-reported emissions from CEMS data. For the Intermountain power plant, the satellite-derived fluxes are within one standard deviation of the prior ensemble mean for most of the days in June and December 2021, resulting in a minor posterior emission update that agrees with CEMS data. A temporary peak in emissions is seen on June 15-19, when CEMS emissions are outside the prior uncertainty range. This peak is also seen in the satellite-derived emissions, which are 2-4× higher than the prior. The posterior emissions are corrected upward by up to a factor 2 on these days, resulting in a close agreement with the reported emissions for the Intermountain power plant during this episode.

For the Thomas Hill Energy Center (Figure 9), reported emissions are larger than the IFS prior for both analysed months. In June, satellite-derived emissions suggest lower emissions within the prior uncertainty range. As a result, the posterior emissions are not substantially different from the prior during this month. During December, there is a better agreement between the satellite-derived and power plant-reported emissions. As a result, the posterior emissions are corrected upward on most days, which results in a better agreement with reported emissions. On individual days (e.g., December 3, 8 and 13), the posterior mean is outside the prior uncertainty range, demonstrating that the prior uncertainty tuning can correct for misrepresented prior emissions or its temporal variability.

Overall, 292 individual hotspot emission estimates were assimilated. For the majority of assimilated hotspot emissions (86%), this resulted in an improved agreement with the assimilated flux. In 52% of the cases, this resulted in reduction of the posterior uncertainty. This due to the low number of posterior fluxes and due to noise resulting from the low IFS ensemble size (Figure 3). The implementation of iterative tuning of σ_b based on cost function evaluation (see Section 3.2) is expected to increase the rate of posterior error reduction.

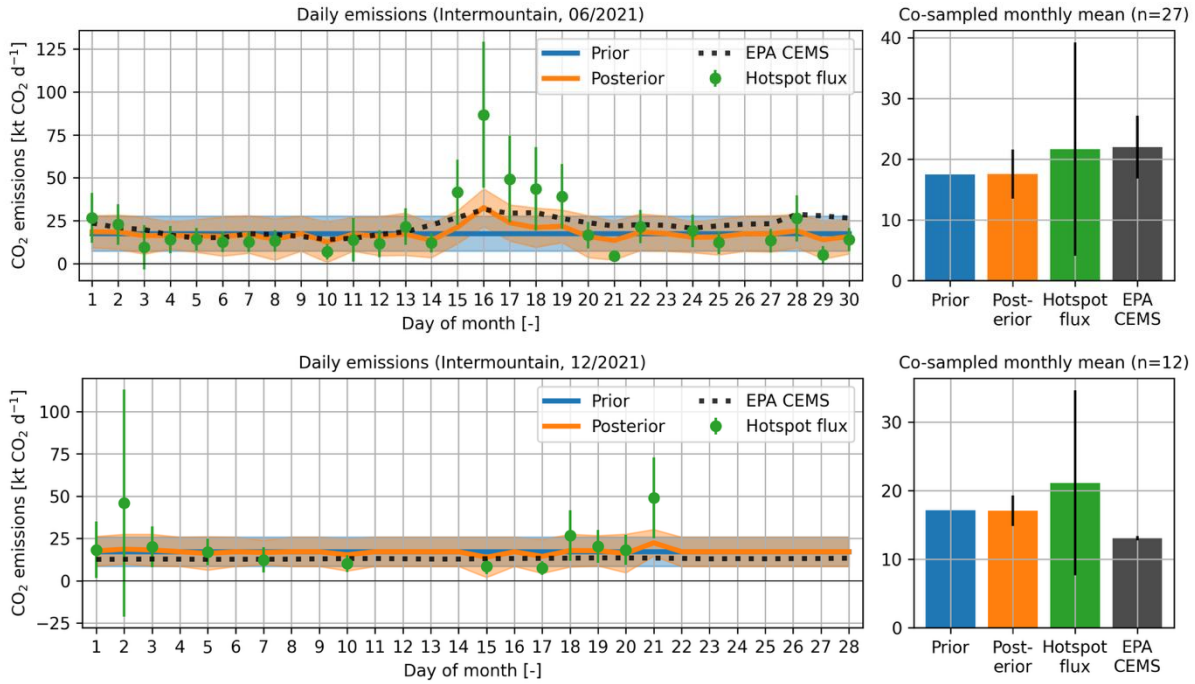

Figure 9. Impact of hotspot assimilation on CO_2 emissions for the Intermountain power plant for June (upper panels) and December (lower panels) 2021, displayed as a time series (left column) and monthly average (right column). Prior and posterior emissions are shown in blue and orange lines and bars, respectively. The green points and bars indicate the assimilated observations, and the black lines and bars indicate the power plant emissions reported to EPA. In the left panels, shaded areas and error bars indicate the ±1σ range. In the right panels, the prior, posterior and EPA CEMS emissions are co-sampled with valid hotspot estimates, and the error bars indicate the standard deviation of daily emissions.

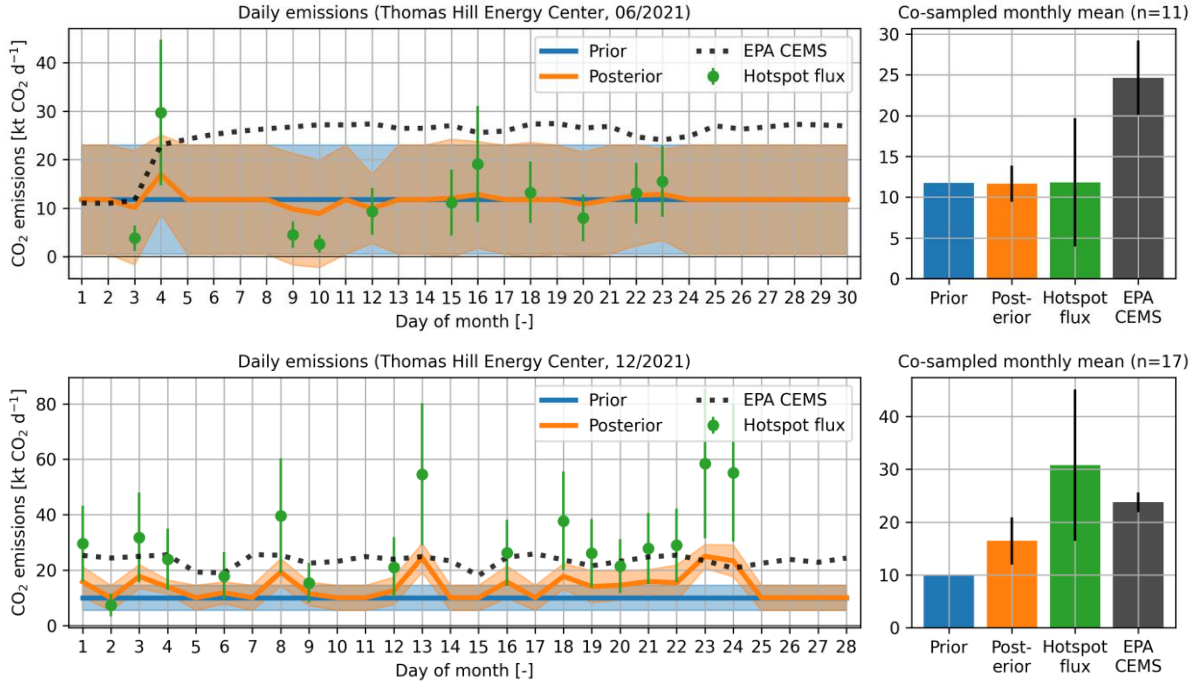

Figure 8. As Figure 9, but for the Thomas Hill Energy Center power plant.

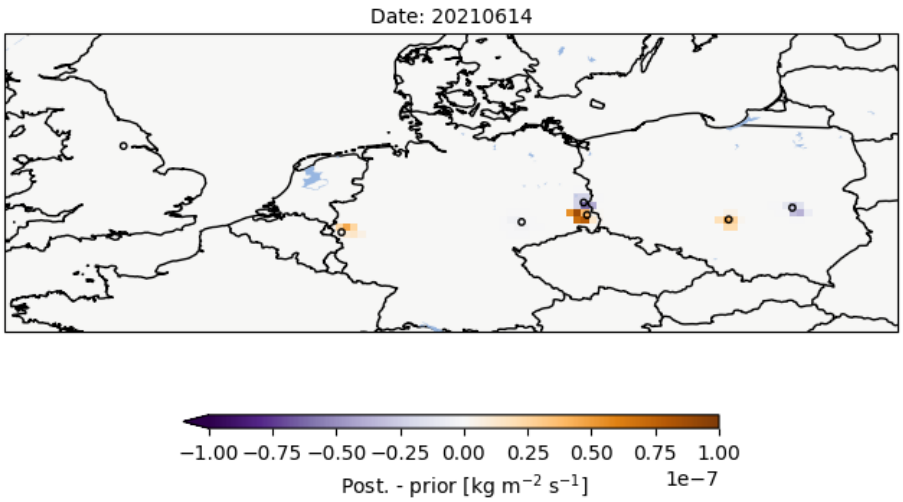

Figure 10. Posterior emission correction because of assimilating TROPOMI-derived hotspot CO_2 emissions on June 14th, 2021, over Europe. The emissions were regridded from the octahedral $T_{co}399$ grid to a regular grid of 0.25°x0.25°. The black circles depict the power plants for which hotspot emission estimates were available from CORSO Deliverable D2.2.

An example of the emission correction after assimilating posterior hotspot CO_2 emissions is shown in Figure 10. The emission corrections are confined to the grid cells containing the power plant and neighbouring grid cells. The IFS prior emissions contain spatial correlation over larger distances, but these were filtered out by applying localization as explained in Section 3.2. This results in fine-scale spatial emission corrections, as evidenced by the corrections of opposite sign for the nearby power plants in Eastern Germany.

4.2 EnKF assimilation results for Europe 2021

An analysis of the EnKF based data assimilation procedure to improve model agreement with observations (TROPOMI NO_2) is presented in Figure 8. As expected, model agreement improves, with an annual overall increase in R^2 of 0.15, a reduction in MAE of 7×10^{13} molec/cm^2, and an EVR of 16%. June and July show the largest improvements in correlation (0.36 and 0.29) and EVR (28% and 29%), likely driven by the maximal number of observations during these months (see Figure 11). In contrast, the largest reduction in MAE occurs in the winter, which coincides with higher atmospheric NO_2 concentrations due to the longer NO_x lifetime and elevated emissions.

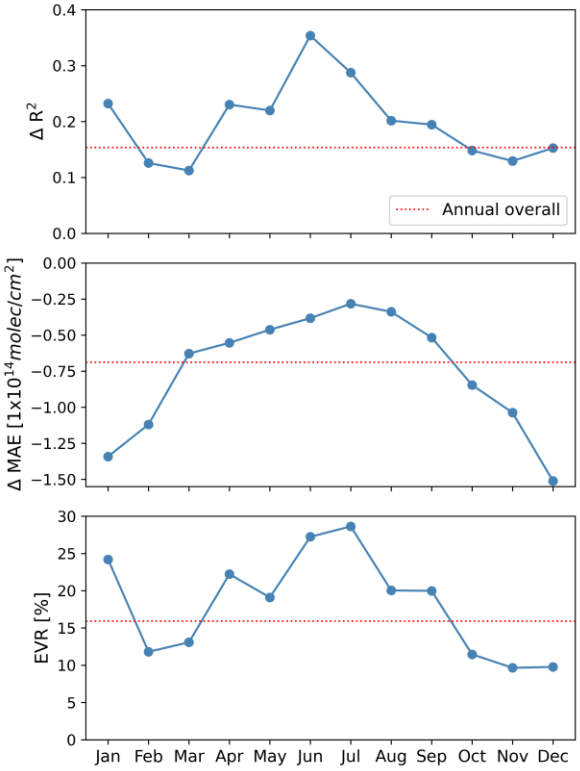

Figure 11. Monthly changes in model agreement with TROPOMI observations resulting from updating prior to posterior NO_x fluxes. Shown are the changes in R^2, MAE, and EVR for each month. The annual overall change in each metric is indicated by the dashed red line.

A comparison of the prior and posterior CO_2 combustion fluxes for Europe in 2021 are shown in Figure 12. We find a consistent reduction in emissions uncertainty from a mean aggregate uncertainty of 96% in the prior, to 32% in the posterior. The fraction of days for which the prior lies within the posterior uncertainty exhibits substantial regional variability from 8% to 66%. Northern and central European countries such as Sweden (66%), Poland (57%), Germany (53%), and Belgium (52%) show the highest levels of prior–posterior consistency. In contrast, southern and southeastern Europe - notably Greece (8%), Turkey (17%), Spain (23%), and Italy (38%) exhibit much poorer agreement. The normalised mean deviation error, which quantifies the typical magnitude of the deviation outside of the prior uncertainty relative to the flux magnitude, ranges from 0.13 to 0.40. Again, a clear geographical contrast emerges with Northern Europe consistently exhibiting smaller deviations (Sweden 0.13, Germany 0.18, Poland 0.18), implying that even when the prior falls outside posterior uncertainty the discrepancy is relatively small. By contrast, Turkey (0.4), Greece (0.33), Spain (0.26), and Hungary (0.26) show substantially larger normalised errors, reflecting stronger corrections by the assimilation.

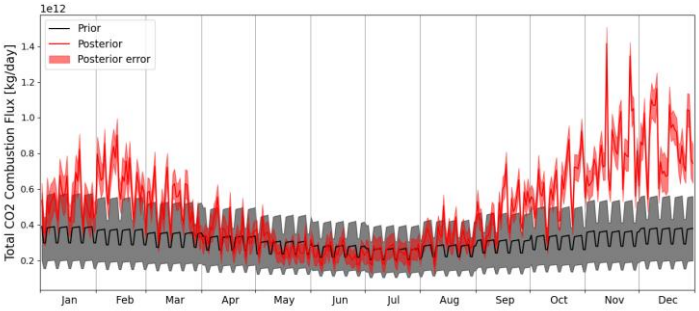

(a)

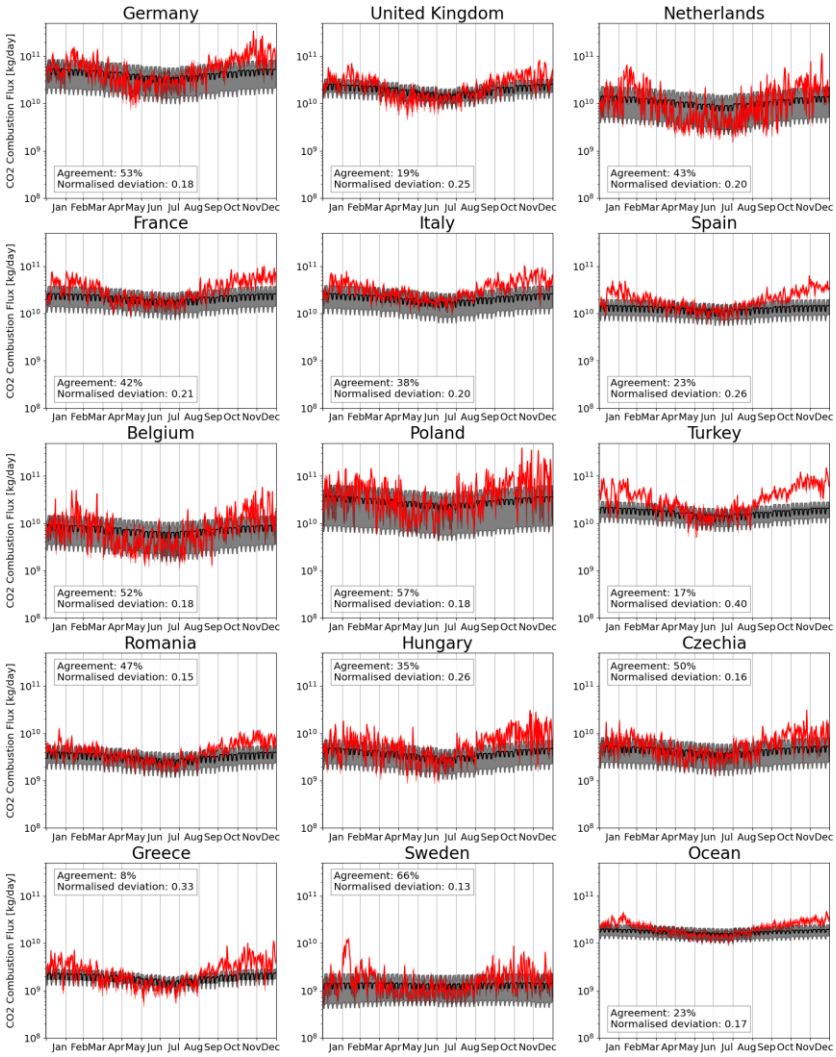

(b)

Figure 12. Prior (grey) and posterior (red) CO_2 combustion fluxes from EnKF assimilation of TROPOMI NO_2 observations over Europe in 2021: (a) total European fluxes and (b) fluxes by the 14 highest-emitting countries and the ocean (shipping). For each country, the agreement (proportion of days where prior and posterior fluxes overlap) and normalised deviation (mean deviation of posterior outside of prior uncertainty, normalised by flux magnitude) are indicated.

It is worth noting that there is relatively strong day-to-day variability in the posterior fluxes. This is likely driven by gaps and inhomogeneities in the observational coverage, which cause intermittent and uneven constraints in the EnKF system and worsens in winter months. Additional contributions may arise from underestimated observation or model–data mismatch uncertainties, retrieval artefacts, and transport model errors, leading to amplified high-frequency noise in the posterior. In practice, the true emissions should be much smoother in time, and a temporally smoothed version of the posterior would likely provide a more realistic estimate.

Visually, the inversion amplifies the seasonal cycle, which is largely driven by higher posterior fluxes during winter months (January, February, November, December) across most countries, but most prevalent in Turkey and Spain. In some countries - specifically the United Kingdom, the Netherlands, Belgium, and Germany - the posterior fluxes see some reductions during spring/summer months. shows the mean monthly increment maps, for which these seasonal shifts are clear. The highest magnitude decreases in emissions are found in northwestern Europe in April and May, while the highest magnitude increases are seen across most of the region in November and December.

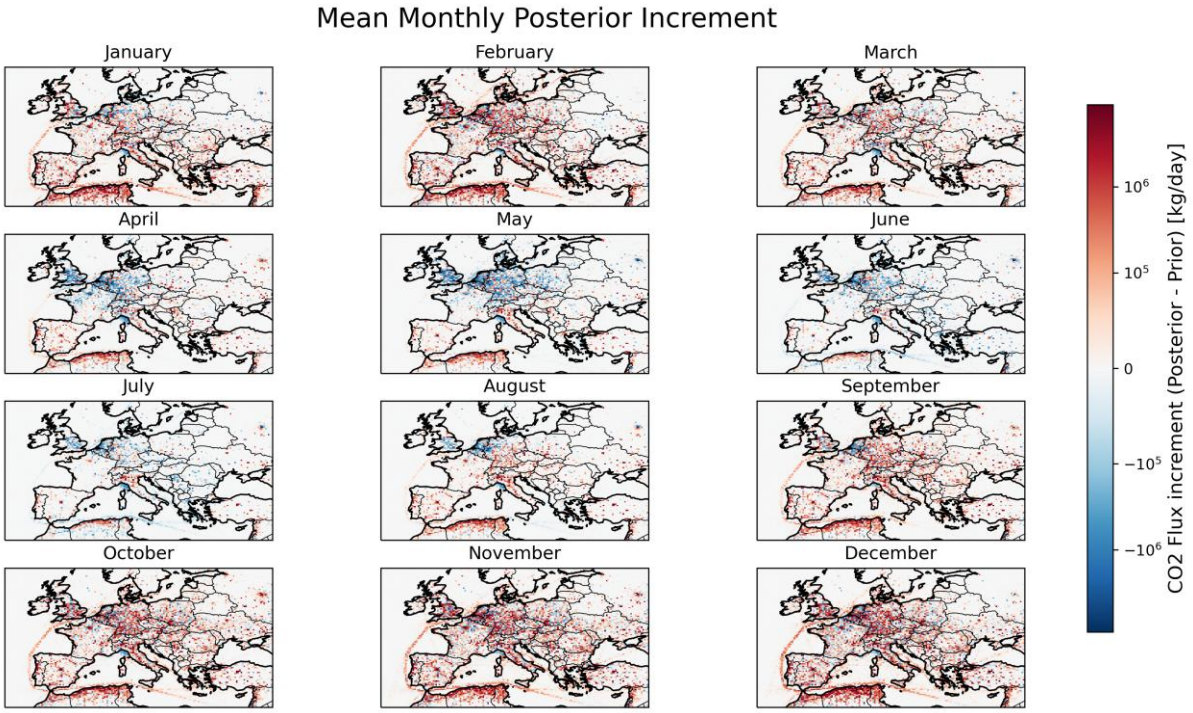

Figure 13. Mean monthly posterior increment maps show the average regional trends of flux changes (red=increase, blue=decrease relative to prior).

4.3 Intercomparison between IFS hotspot-assimilated and GEOS-Chem posterior CO_2 emissions for European power plants

As a final step, we compare emission estimates from both assimilation procedures discussed in this report. The two methods are not necessarily expected to fully agree in their posterior flux estimates due to differences in spatial resolution between GEOS-Chem and IFS and the different setup of the control vectors (GEOS-Chem adjusts all anthropogenic sectors while the IFS hotspot assimilation only targets the energy sector). To minimise these effects, we only included five out of eight European power plants that have valid hotspot observations and where the contribution of the energy sector to the total emission is >75% on the GEOS-Chem grid. Additionally, we only focus on June, since there are only 1-3 hotspot observations for each power plant during December.

Two examples of this comparison between both systems are shown in Figure 14. For the ENEA power plant (upper panels in Figure 14), the IFS posterior emissions are within the prior uncertainty, owing to the relatively high prior uncertainty and observation uncertainties. GEOS-Chem posterior fluxes are largely unchanged with respect to the prior for most days of the month. On some days, the assimilation results in a strong downward correction of GEOS-Chem posterior emissions to within the IFS uncertainty range. For the Boxberg power plant (lower panels in Figure 14), GEOS-Chem posterior emissions are largely unchanged with respect to the prior on most days. Hotspot assimilations into the IFS leads to a large increase in emissions, resulting in a better agreement with the GEOS-Chem posterior on days with valid fluxes. The agreement between GEOS-Chem and the IFS hotspot assimilation procedure on individual is encouraging, but more targeted experiments would be required to obtain more quantitative understanding of the performance of both methods.

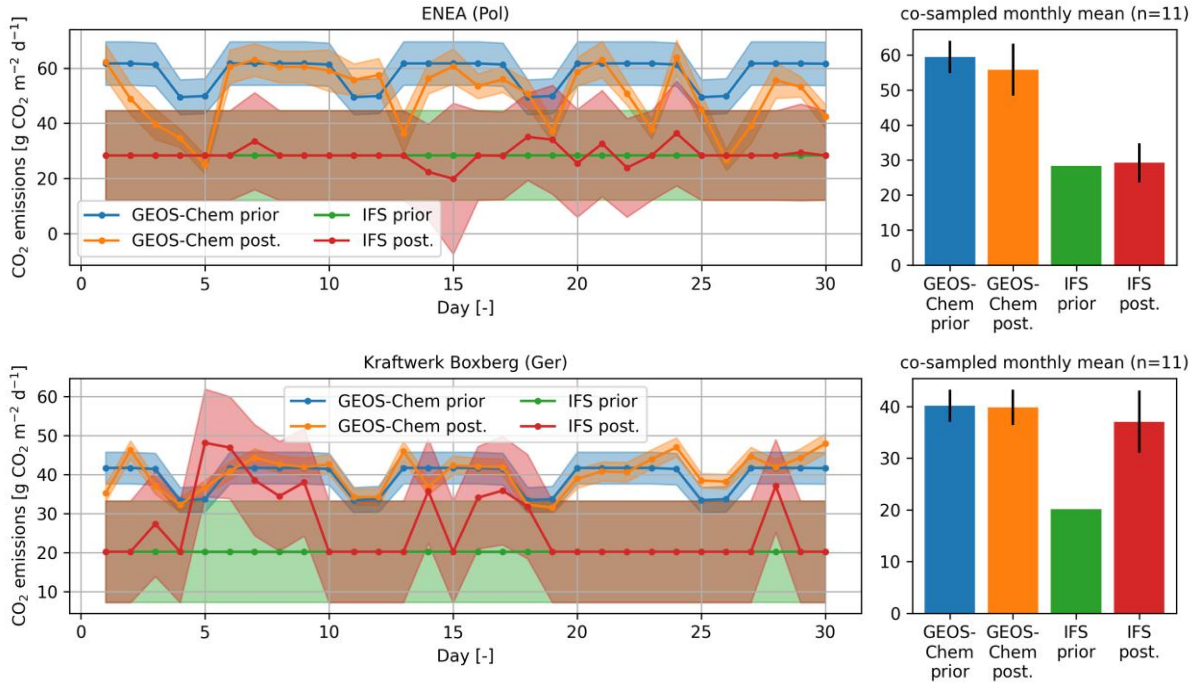

Figure 14. Comparison of prior and posterior emissions between GEOS-Chem and the IFS-based posterior flux assimilation procedure for two European power plants in June 2021. Left panels shows the time series for this month (solid lines and shaded areas represent the daily mean and ±1σ range, respectively). The right panels display the monthly mean of both prior and posterior emission estimates, co-sampled with valid hotspot observations. Error bars indicate the standard deviation of the mean.

5 Conclusion

This deliverable describes the methodology and implementation of the posterior flux assimilation methodology (Bousserez, 2019) to apply posterior corrections to IFS inversion results, as well as the further development of an Ensemble Kalman Filter inversion system in GEOS-Chem.

The posterior flux assimilation methodology was first tested in a range of OSSE experiments, in which synthetic observations are generated from the ensemble control member, perturbed with an assumed uncertainty, and subsequently assimilated. This provided insights into the dependence of posterior uncertainty on ensemble size and potential misrepresentations in the assumed prior uncertainty. The ensemble-derived uncertainty is underestimated with respect to the approximated true uncertainty for small ensemble sizes. Additionally, the inversion approach cannot fully recover the posterior uncertainty starting from a wrongly specified prior uncertainty. Correcting mis-represented prior uncertainties requires an adaptive prior uncertainty tuning approach, which has been introduced as part of this deliverable.

The posterior flux assimilation methodology was tested by assimilating hotspot CO_2 emission estimates, derived from TROPOMI NO_2 observations, into a posterior emission ensemble using a total of 252 hotspot emission estimates for 17 power plants in the United States and Europe. The hotspot assimilation algorithm results in reduced mismatch with the assimilated observations. Additionally, we have presented case studies where assimilation of satellite-derived hotspot CO_2 emissions improves the magnitude and temporal variability in posterior emissions compared to power-plant-reported emissions.

The EnKF-based data assimilation clearly improves agreement between the model and TROPOMI NO_2 observations, reducing flux uncertainties and correcting prior CO_2 combustion fluxes across Europe. Northern and central Europe generally exhibit better prior–posterior consistency and smaller normalized deviations, while southern and southeastern regions require larger corrections, particularly during winter months. Posterior fluxes also show pronounced day-to-day variability, likely reflecting gaps in observational coverage, uneven constraints, and model–data mismatch uncertainties. Overall, the assimilation amplifies the seasonal cycle, with increased posterior fluxes in winter and reduced fluxes in spring and summer in several countries. Overall, these results highlight the advantage of the parameterised offline NO_x chemistry in GEOS-Chem, which enables an efficient assimilation procedure without the need for computationally intensive full-chemistry ensemble runs.

Future developments to the hotspot emission assimilation methodology include implementation of an adaptive prior uncertainty tuning approach based on cost function evaluation, application to other species (e.g., methane and NO_x) and implementation of log-normal uncertainty distribution. A further element that requires investigation is the use of hotspot emission assimilation on days without valid emission estimates (e.g. due to cloud cover limiting the detection of emission plumes), e.g. by using assumptions on emission persistence (Jervis et al., 2025). Further validation of hotspot emission estimates could be performed based on power plant-reported emissions in other regions (e.g., Tang et al., 2020). Additionally, the online implementation of this assimilation algorithm in the IFS requires satellite observation filtering (to avoid double use of the same satellite observations in the conventional 4D-Var assimilation and for the hotspot emission assimilation algorithm) and including the updated emissions (after hotspot assimilation) in the IFS forward model. This work is already underway as part of other activities within CAMS.

A recommendation for further work of the regional GEOS-Chem inversion system is to develop multi-species inversions combining CO_2 and NO_2 observations, which are expected to further constrain fluxes and improve spatial and temporal accuracy. Refinement of the CO_2:NO_x emission ratio will also be necessary to improve results. Additionally, further validation using

in situ NO_2 networks and CO_2 observations, as well as exploration of other influencing factors such as temperature and meteorology, could be carried out to better understand remaining discrepancies and improve inversion robustness.

6 References

Agusti-Panareda, A., Diamantakis, M., Bayona, V., Klappenbach, F., and Butz, A. (2017). Improving the inter-hemispheric gradient of total column atmospheric CO_2 and CH_4 in simulations with the ECMWF semi-Lagrangian atmospheric global model, Geosci. Model Dev., 10, 1–18, https://doi.org/10.5194/gmd-10-1-2017.

Agustí-Panareda, A., McNorton, J., Balsamo, G. et al. (2022). Global nature run data with realistic high-resolution carbon weather for the year of the Paris Agreement. Sci. Data 9 (160), https://doi.org/10.1038/s41597-022-01228-2.

Bechtold, P., Semane, N., Lopez, P., Chaboureau, J.-P., Beljaars, A., Bormann, N. (2014). Representing equilibrium and nonequilibrium convection in large-scale models, J. Atmos. Sci., 71, 734-753, https://doi.org/10.1175/JAS-D-13-0163.1.

Bey, I., Jacob, D. J., Yantosca, R. M., Logan, J. A., Field, B. D., Fiore, A. M., Li, Q., Liu, H. Y., Mickley, L. J., & Schultz, M. G. (2001). Global modeling of tropospheric chemistry with assimilated meteorology: Model description and evaluation. *Journal of Geophysical Research: Atmospheres, 106*(D19), 23073–23095. https://doi.org/10.1029/2001JD000807

Bousserez, N. (2019). Towards a prototype global CO_2 emissions monitoring system for Copernicus, arXiv preprint, https://arxiv.org/abs/1910.11727.

Chapnik, B., Desroziers, G., Rabier, F., Talagrand, O. (2006). Diagnosis and tuning of observational error in a quasi-operational data assimilation setting. *Quarterly Journal of the Royal Meteorological Society*, 132(615), p. 543–565, https://doi.org/10.1256/qj.04.102.

Courtier, P., Thépaut, J.-N., and Hollingsworth, A. (1994). A strategy for operational implementation of 4D-Var, using an incremental approach, Q. J. Roy. Metrotol. Soc., 120, 1367–1387, https://doi.org/10.1002/qj.49712051912.

Diamantakis, M., Magnusson, L. (2016). Sensitivity of the ECMWF model to semi-Lagrangian departure point iterators, Mon. Weather Rev., 144(9), https://doi.org/10.1175/MWR-D-15-0432.1.

Environmental Protection Agency (2025). Clean Air Markets Program Data. https://campd.epa.gov/data/custom-data-download. (last access: 5 December 2025).

Flemming, J., Huijnen, V., Arteta, J., Bechtold, P., Beljaars, A., Blechschmidt, A.-M., Diamantakis, M., Engelen, R. J., Gaudel, A., Inness, A., Jones, L., Josse, B., Katragkou, E., Marecal, V., Peuch, V.-H., Richter, A., Schultz, M. G., Stein, O., and Tsikerdekis, A. (2015). Tropospheric chemistry in the Integrated Forecasting System of ECMWF, Geosci. Model Dev., 8, 975–1003, https://doi.org/10.5194/gmd-8-975-2015.

Feng, L., Palmer, P. I., Bösch, H., and Dance, S. (2009) Estimating surface CO2 fluxes from space-borne CO2 dry air mole fraction observations using an ensemble Kalman Filter, *Atmospheric Chemistry and Physics,* 9, p. 2619–2633, https://doi.org/10.5194/acp-9-2619-2009.

Feng, L., Palmer, P. I., Bösch, H., Parker, R. J., Webb, A. J., Correia, C. S., Deutscher, N. M., Domingues, L. G., Feist, D. G., Gatti, L. V., et al. (2017). Consistent regional fluxes of CH_4 and CO_2 inferred from GOSAT proxy XCH_4: XCO_2 retrievals, 2010–2014, *Atmospheric Chemistry and Physics*, 17, 4781–4797, https://doi.org/10.5194/acp-17-4781-2017.

Gaspari, G., Cohn, S.E. (1999). Construction of correlation functions in two and three dimensions. *Quarterly Journal of the Royal Meteorological Society*, 125, p. 723-257, doi: https://doi.org/10.1002/qj.49712555417.

Gressent, A., Sauvage, B., Cariolle, D., Evans, M., Leriche, M., Mari, C., and Thouret, V. (2016). Modeling lightning-NOx chemistry on a sub-grid scale in a global chemical transport

model. *Atmospheric Chemistry and Physics*, 16, p. 5867–5889. https://doi.org/10.5194/acp-16-5867-2016.

Guevara, M., Val, A., Collado, O., Dellaert, S., Denier van der Gon, H. (2024). Improved global point source emission dataset. CORSO Deliverable report D1.2, https://www.corso-project.eu/sites/default/files/2025-02/CORSO-D1-2-V1.1.pdf.

Hersbach, H., Bell, B., Berrisford, P., Hirahara, S., Horányi, A., Muñoz-Sabater, J., Nicolas, J., Peubey, C., Radu, R., Schepers, D., Simmons A., Soci, C., Abdalla, S. Abellan, X., Balsamo, G., Bechtold, P., Biavati, G., Bidlot, J., Bonavita, M., De Chiara, G., Dahlgren, P., Dee, D., Diamantakis, M., Dragani, R., Flemming, J., Forbes, R., Fuentes, M., Geer, A., Haimberger, L., Healy, S., Hogan, R.J., Hólm, E., Janisková, M., Keeley, S., Laloyaux, P., Lopez, P., Lupu, C., Radnoti, G., De Rosnay, P., Rozum, I., Vamborg, F., Villaume, S., and Thépaut, J-N. (2020). The ERA5 global reanalysis, *Quarterly Journal of the Royal Meteorological Society,* 146, p. 1999-2049, doi: https://doi.org/10.1002/qj.3803.

Hohenberger, T. L., Malki, M. E., Visschedijk, A., Guevara, M., Ramacher, P., Marongiu, A., Lanzani, G. G., Fossati, G., Kousa, A., Athanasopoulou, E., Kakouri, A., & Kuenen, J. (2025). Link-based European road transport emissions for CAMS-REG v8.1 and a comparison to city inventories, *Earth System Science Data Discuss.* [preprint], https://doi.org/10.5194/essd-2025-428.

Jervis, D., Girard, M., MacLean, J.W., Marshall, D., McKeever, J., Strupler, M., Ramier, A., Tarrant, E., Young, D., Maasakkers, J.D., Aben, I., Scarpelli, I. (2025). Global energy sector methane emissions estimated by using facility-level satellite observations. *Science*, 390(6778), p. 1151-1155, doi: https://doi.org/10.1126/science.adv3183.

Kuhlmann, G., Henne, S., Meijer, Y., Brunner, D. (2021). Quantifying CO_2 emissions of power plants with CO_2 and NO_2 imaging satellites. *Frontiers in Remote Sensing*, 2., article no. 689838, https://doi.org/10.3389/frsen.2021.689838.

Kuhlmann, G., Koene, E., Meier, S., Leguijt, G., Segers, A., Denier van der Gon, H., Schooling, C., Finch, D., and Palmer, P. (2025). Time series of NO_x and CO emissions of hot spots in Africa, Europe and SE Asia in reference year. CORSO Deliverable report D2.2, https://www.corso-project.eu/sites/default/files/2025-10/CORSO-D2-2-V1.1.pdf.

Liu, F., Duncan, B. N., Krotkov, N. A., Lamsal, L. N., Beirle, S., Griffin, D., McLinden, C. A., Goldberg, D. L., and Lu, Z. (2020). A methodology to constrain carbon dioxide emissions from coal-fired power plants using satellite observations of co-emitted nitrogen dioxide, Atmos. Chem. Phys., 20, 99–116, https://doi.org/10.5194/acp-20-99-2020.

McNorton, J., Bousserez, N., Agustí-Panareda, A., Balsamo, G., Cantarello, L., Engelen, R., Huijnen, V., Inness, A., Kipling, Z., Parrington, M., and Ribas, R. (2022). Quantification of methane emissions from hotspots and during COVID-19 using a global atmospheric inversion, Atmos. Chem. Phys., 22, 5961–5981, https://doi.org/10.5194/acp-22-5961-2022.

Rabier, F., Järvinen, H., Klinker, E., Mahfouf, J.-F., and Simmons, A.: The ECMWF operational implementation of four-dimensional variational assimilation. I: Experimental results with simplified physics, Q. J. Roy. Meteorol. Soc., 126, 1143–1170, https://doi.org/10.1002/qj.49712656415, 2000.

Sandu, I., Beljaars, A., Bechtold, P., Mauritsen, T., Balsamo, G. (2013). Why is it so difficult to represent stably stratified conditions in numerical weather prediction (NWP) models?, J. Adv. Model. Earth Syst., 5, 117-133, https://doi.org/10.1002/jame.20013.

Schooling, C. N., Palmer, P. I., Visser, A., & Bousserez, N. (2025). Development of a parametrised atmospheric NOx chemistry scheme to help quantify fossil fuel CO_2 emission estimates. *Atmospheric Chemistry and Physics*, 25(22), p. 15631-15652. https://doi.org/10.5194/acp-25-15631-2025.

Soulie, A., Granier, C., Darras, S., Zilbermann, N., Doumbia, T., Guevara, M., Jalkanen, J.-P., Keita, S., Liousse, C., Crippa, M., Guizzardi, D., Hoesly, R., and Smith, S. J. (2024). Global anthropogenic emissions (CAMS-GLOB-ANT) for the Copernicus Atmosphere Monitoring Service simulations of air quality forecasts and reanalyses, Earth Syst. Sci. Data, 16, 2261–2279, https://doi.org/10.5194/essd-16-2261-2024.

Tang, L., Xue, X., Qu, J. et al. (2020). Air pollution emissions from Chinese power plants based on the continuous emission monitoring systems network. Sci. Data, 7 (325), https://doi.org/10.1038/s41597-020-00665-1.

Veefkind, J.P., Aben, I., McMullan, K., Förster, H., De Vries, J., Otter, G., Claas, J., Eskes, H.J., De Haan, J.F., Kleipool, Q., Van Weele, M., Hasekamp, O., Hoogeveen, R., Landgraf, J., Snel, R., Tol, P., Ingmann, P., Voors, R., Kruizinga, B., Vink, R., Visser, H., and Levelt, P.F. (2012). TROPOMI on the ESA Sentinel-5 Precursor: A GMES mission for global observations of the atmospheric composition for climate, air quality and ozone layer applications. *Remote Sensing of Environment*, 120, p. 70-83, doi: https://doi.org/10.1016/j.rse.2011.09.027.

Vinken, G. C. M., Boersma, K. F., Maasakkers, J. D., Adon, M., and Martin, R. V. (2014) Worldwide biogenic soil NOx emissions inferred from OMI NO2 observations. *Atmospheric Chemistry and Physics*, 14(10), p. 363–381. https://doi.org/10.5194/acp-14-10363-2014.

Document History

Version	Author(s)	Date	Changes
0.1	A.J. Visser, C. Schooling, N. Bousserez, P. Palmer	05-12-2025	
1.0	A.J. Visser, C. Schooling, N. Bousserez, P. Palmer	17-12-2025	Addressed feedback provided by the internal reviewers

Internal Review History

Internal Reviewers	Date	Comments
Marko Scholze (ULUND) and Jean-Christophe Calvet (MeteoFrance)	December 2025	